A bimetallic metal–organic framework derived MnS/CoS@C heterostructure with enhanced sodium-ion storage†

Zongyuan Jiang, [iD] ‡[a] Shaohui Li, [iD] ‡[b] Yining Chen,[b] Jingwei Chen, [iD] [c] Cong Wei [iD] *[b] and Qun Xu [iD] *[a,b]

Manganese sulfide (MnS) has gained significant attention as a high capacity and durable anode material for sodium-ion batteries (SIBs) due to its high theoretical capacity and decent redox reversibility. However, sluggish Na^+ diffusion and significant volume variation during charge/discharge cycles limited its rate capability and cycling stability. Here, a new MnS/CoS heterojunction embedded in S-doped carbon (MnS/CoS@C) is designed through sulfurization of a bimetallic metal–organic framework (MOF). The synergistic effect of heterojunction design and carbon framework encapsulation integrates several benefits, including facilitating ion/electron transport, alleviating volume variation, and preventing the agglomeration of metal sulfide nanoparticles. Therefore, the MnS/CoS@C composite manifests remarkable rate capability (526.1 mA h g^{-1} at 0.1 A g^{-1} and 273.7 mA h g^{-1} at 10 A g^{-1}) and stable long-term cycle life (214.8 mA h g^{-1} after 1000 cycles at 5 A g^{-1}). Meanwhile, the sodium storage mechanism is examined using *in situ* electrochemical impedance spectroscopy (EIS), *ex situ* X-ray diffraction (XRD) and *ex situ* X-ray photoelectron spectroscopy (XPS). Coupled with a carbon nanosheet cathode, a prototype sodium-ion capacitor (SIC) has been fabricated. The SIC can achieve a high energy density of 120.7 W h kg^{-1} and a maximum power density of 12 250 W kg^{-1}, demonstrating the high application potential of the composite for sodium-ion based energy storage systems.

Introduction

As energy and environmental issues become more prominent, harvesting green and clean energy has become imperative. Renewable energy sources, including wind, solar, and geothermal, are widely used. However, the geographical and intermittent nature of these sustainable energy sources limits their direct use at the grid scale, requiring grid-level energy storage systems (EESs) to support their application.[1] Lithium-ion batteries (LIBs) have been widely used in our daily lives, including in portable electronics and EESs.[2,3] Unfortunately, the limited reserves on the Earth and the rising cost of lithium restrict its further progression in grid-level EESs. In this respect, rechargeable sodium-ion batteries (SIBs) are considered as a

potential replacement for LIBs owing to their Earth-abundant resources, the even distribution of sodium and similar operating mechanisms.[4,5] Nevertheless, their development still faces serious problems, such as large volume changes and slow reaction kinetics due to the larger diameter of Na^+, resulting in inferior rate performance and cycling stability. Therefore, there is an urgent need to create and accurately design high electrochemical performance anode materials for SIBs.[6–8]

Transition metal sulfides (TMSs) have garnered widespread attention as novel anode materials in SIBs because of their high theoretical capacity, controllable morphologies/nanostructures, relatively weak M–S bonding strength and unique electrochemical properties.[9] Until now, numerous metal sulfides (M_xS_y = Fe, Co, Ni, Cu, Mn, *etc.*) have been explored as anodes for SIBs and great progress has been achieved.[10–12] Among them, manganese sulfide (MnS) has been extensively explored as an SIB anode candidate owing to its high theoretical specific capacity (616 mA h g^{-1}) and suitable electrochemical reaction platform. However, they still suffer from severe volume change, intrinsic poor conductivity and the polysulfide shuttle effect, resulting in inferior rate capacity and inadequate cycle life.[13] To circumvent these problems, numerous strategies have been adopted from other rechargeable batteries. (1) Constructing micro/nanostructures with interior

[a]*Henan Institute of Advanced Technology, Zhengzhou University, Zhengzhou, 450001, P. R. China. E-mail: Qunxu@zzu.edu.cn*
[b]*School of Materials Science and Engineering, Zhengzhou University, Zhengzhou, 450001, P. R. China. E-mail: weicong@zzu.edu.cn*
[c]*School of Materials Science and Engineering, Ocean University of China, Qingdao, 266100, P. R. China*
†Electronic supplementary information (ESI) available. See DOI: https://doi.org/10.1039/d3nr01618h
‡These two authors contributed equally to this work.

space, which can efficiently accelerate ion/electron migration and alleviate volume changes; (2) forming composites with conductive heteroatom (such as S, N, and P) doped carbonous materials, which can promote charge transport, maintain structural integrity, and impede the dissolution of polysulfides.[8,14–19] So far, most of the work has focused on the two perspectives mentioned above, with the aim of promoting the diffusion kinetics. As expected, significant progress has been made in recent years on MnS-based anode materials, but the comprehensive properties are still unsatisfactory. In addition, little research has been done on regulating the internal crystal structure of MnS materials to further enhance the ionic/electronic transport kinetics.

Recently, binary metal sulfides with heterojunction structures have caught many researchers' attention owing to their significant advantages in sodium storage, such as WS_{2-x}/ZnS@C,[20] Sb_2S_3@FeS$_2$ [21] hollow nanorods and SnS_2/Co$_3$S$_4$ hollow nanocubes.[22] The interface between different components could induce an internal electric field and increase the number of active sites, resulting in improved electrochemical properties.[11,23–25] Nonetheless, the passivation of the interfacial reaction and the dissolution of polysulfide intermediates still retard the reaction kinetics during the repeated sodiation/desodiation process. In addition, the scrupulous and accurate design of highly integrated and uniformly distributed heterostructure electrodes remains a challenge that needs to be resolved.

Herein, an octahedral structure of MnS/CoS heterojunctions homogeneously encapsulated in S-doped carbon (denoted as MnS/CoS@C) was precisely designed by using Mn- and Co-based bimetallic metal–organic frameworks (MOFs) as starting materials. The formed S-doped carbon shell derived from organic ligands can mitigate the volume variation, inhibit the aggregation of MnS/CoS nanoparticles caused by Na$^+$ insertion/extraction, and improve the kinetics of ion/electron migration,[26] while the heterojunction of MnS and CoS could generate internal built-in electric fields that greatly enhance the interfacial reaction kinetics and ion/electron migration. Benefiting from its hierarchical structure, the as-produced MnS/CoS@C composite can yield an ultrahigh initial capacity (526.1 mA h g^{-1} at 0.1 A g^{-1}), excellent rate performance (273.7 mA h g^{-1} at 10 A g^{-1}) and cycling durability (84.7% capacity retention after 1000 cycles). The electrochemical Na$^+$ storage behavior of MnS/CoS@C was also characterized by *in situ* EIS, *ex situ* XRD and *ex situ* XPS. In addition, a prototype sodium-ion capacitor (SIC) composed of the MnS/CoS@C anode and the N-doped carbon nanosheet (NC) cathode can demonstrate a remarkable energy density of 120.7 W h kg^{-1} and a superior high-power density of 12 250 W kg^{-1}.

Experimental

Material preparation

Synthesis of Mn-MIL-100 octahedra. A modified solvothermal method was used to prepare Mn-MIL-100 precursors. At first, 120.5 mg of Mn(NO$_3$)$_2$·4H$_2$O, 0.399 mg of trimesic acid (C$_6$H$_3$(COOH)$_3$), and 1.8 g of lauric acid are dissolved in 50 ml of methanol for 10 minutes. The resulting mixture is then sealed in a 100 ml autoclave reactor and kept at 125 °C for 6 hours. After cooling down naturally, the sediment is separated by centrifugation and rinsed several times with ethanol. The brown Mn-MIL-100 product is then dried in a vacuum at 60 °C.[27]

Synthesis of Co/Mn-MIL-100 octahedra. Similar to the above method, Co/Mn-MIL-100 octahedra were prepared except that 46.5, 93.12, and 139.7 mg of Co(NO$_3$)$_2$·6H$_2$O are added to the solution before the solvothermal process, respectively.

Synthesis of the Co–BTC MOF. 1.68 g of trimesic acid was dissolved evenly in 100 mL of anhydrous ethanol, and then 100 mL of water and 3.49 g of Co(NO$_3$)$_2$·6H$_2$O were added. When the dissolution was completed, 0.96 g of NaOH was added. After 30 minutes of stirring, the resulting mixture was centrifuged and the sediment was rinsed several times using deionized water and ethanol, respectively. Finally, a pink powder was obtained after drying at 70 °C for 12 hours under vacuum.

Synthesis of the MnS@C composite, MnS/CoS@C composite and CoS@C composite. Mn-MIL-100, Co/Mn-MIL-100, and Co–BTC were synthesized and transferred to a tubular furnace. The composites were then pre-carbonized at a temperature of 600 °C for 2 hours at a ramping speed of 5 °C min^{-1} under a flow of Ar. To obtain the metal sulfide composite, the pre-carbonized products and sulfur powder with a mass ratio of 1:2 were placed in two separate positions in the furnace. Finally, the samples were sulfurized at 600 °C for 2 hours. The obtained products were named MnS/C composites, MnS/CoS/C (with different Mn/Co ratios) composites, and CoS/C composites.

Electrochemical measurements

To create working electrodes, a slurry was mixed with a 7:2:1 ratio of active materials:conductive additive (Ketjen black):adhesive (polyvinylidene fluoride). *N*-Methyl pyrrolidone (NMP) was selected as the solvent. The obtained slurry was cast onto the current collector and dried completely. The average mass loading of the active material was about 1 mg cm^{-2}. Batteries were assembled and disassembled in an Ar filled glove box. In the electrochemical test, pure sodium metal was applied as both reference and counter electrodes, a GF/D glass membrane was selected as the separator, and 1 M NaPF$_6$ in diethylene glycol dimethyl ether was selected as the electrolyte. The CV curve and EIS were tested using a SP-150 electrochemical workstation. The cycle life and rate performance were determined using a Neware battery testing system. In the galvanostatic intermittent titration technique (GITT) test, the discharge time and relaxation time were 1200 s and 1800 s, respectively, and the current was fixed at 0.1 A g^{-1}. Before fabricating the SIC, the MnS/CoS@C11 anode needed to be pre-treated by sodiation (discharge/charge three times and discharged to 0.01 V).

Material characterization

A field-emission scanning electron microscope (FESEM, ZEISS Sigma 300) was employed to visualize the morphology and nanoscale structure of the sample and a transmission electron microscope (TEM, JEOL JEM 2800) was used to observe the existence of heterojunctions. XRD (Rigaku Smart Lab SEXRD) and XPS (Thermo Scientific ESCALAB 250Xi) analyses were conducted to determine the composition and sodium storage mechanism of the material.

Results and discussion

The schematic diagram of the preparation process of the MnS/CoS@C heterostructured composite material is displayed in Fig. 1a. Briefly, tetrahydrate manganese nitrate and hexahydrate cobalt nitrate are used as metal sources, while benzene-1,3,5-tricarboxylic acid (BTC) is used as an organic ligand to synthesize octahedral Mn/Co-MIL-100 MOFs by a one-step solvothermal method. The MnS/CoS@C heterostructure composite is prepared by a two-step carbonization and sulfurization process. A series of composite materials with different molar ratios of Mn to Co were synthesized and denoted as MnS@C, MnS/CoS@C31, MnS/CoS@C32, MnS/CoS@C11, and CoS@C. Fig. 1b and S1† show the XRD patterns of MnS@C, MnS/CoS@C31, MnS/CoS@C32, MnS/CoS@C11, and CoS@C. All diffraction peaks of pure MnS@C and CoS@C samples can match well with standard cards (JCPDS no. 01-1089 and no. 19-0365).[28,29] For the MnS/CoS@C11 sample, it can be ascribed to the coexistence of MnS and CoS; no other peaks are found, which proves that a high purity MnS and CoS composite was synthesized by carbonization and sulfurization. Fig. 1c and Fig. S2a–c† depict the field-emission scanning electron microscopy (FESEM) images of Mn-MIL-100, Mn/Co-MIL-100-31, Mn/Co-MIL-100-32 and Mn/Co-MIL-100-11 MOF precursors. Obviously, the MOFs exhibit a uniform and regular octahedral shape, while the Co–BTC MOF presents a rectangular structure (Fig. S2d†). As displayed in Fig. 1d and S3, S4,† the carbonation and sulfurization products maintained the original shape of the MOF, and the final size was slightly reduced due to the decomposition and collapse of the organic ligand in the MOF. Compared with the smooth surface of the MOF, the final product demonstrates a roughened surface with some evenly anchored nanoparticles. The organic ligand-derived carbon skeleton can effectively prevent the aggregation of metal sulfides and mitigate the volume changes during the repeated sodiation/desodiation process.

The transmission electron microscopy (TEM) image of MnS/CoS@C11 further proved that all the metal sulfide nanoparticles are homogeneously dispersed in the carbon framework (Fig. 1e and S5a†). The carbon framework can not only enhance the ionic conductivity of the composite but can also prevent the aggregation of the nanoparticles and buffer the volume changes during discharge/charge cycles. In addition,
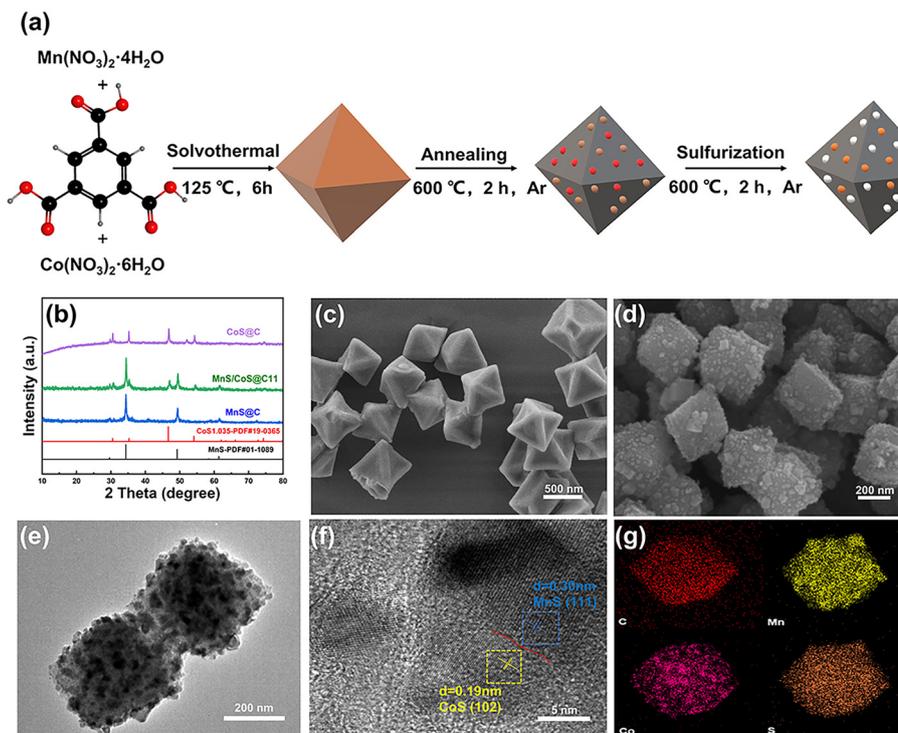

Fig. 1 (a) Schematic of the synthesis of the MnS/CoS@C heterostructure. (b) XRD patterns of MnS@C, MnS/CoS@C11 and CoS@C. (c) SEM images of the Mn/Co-MIL-100-11 MOF. (d) SEM image of MnS/CoS@C11. (e) TEM and (f) HRTEM images of MnS/CoS@C11. (g) TEM-EDX mapping of the MnS/CoS@C11 heterostructure.

the typical high-resolution TEM image (Fig. 1f) shows that the MnS and CoS components are in close contact with the interface, confirming the presence of abundant and robust MnS/CoS heterostructures. The lattice fringes of 0.30 and 0.19 nm are in good agreement with the (111) crystal plane of MnS and the (102) crystal plane of CoS, respectively. As shown in Fig. S5b,† the selected area electron diffraction (SAED) pattern (Fig. S5b†) clearly presents the (100) and (201) planes from CoS and the (220) and (200) planes from MnS. These results demonstrate the formation of the MnS/CoS heterostructure in the carbon matrix, which can induce an internal built-in-electric field, thus boosting the ion/electron transport and promoting the interfacial reaction. The elemental mappings of C, Mn, Co, and S in the MnS/CoS@C11 composite are shown in Fig. 1g. Obviously, all the elements are homogeneously distributed throughout the octahedral structure of the carbon skeleton, which is beneficial for improving the utilization of CoS and MnS, boosting the sodium storage performance. In addition, based on thermogravimetric analysis (TGA) curves, the carbon contents in MnS@C, MnS/CoS@C11 and CoS@C composites are calculated to be 23.5%, 7.8% and 5.3%, respectively (Fig. S6†).

As demonstrated in Fig. 2a–e, the surface chemistry and elemental valence states of MnS/CoS@C11 were examined using XPS analysis. The full XPS spectrum depicted in Fig. 2a demonstrates the presence of Mn, Co, S, and C elements, agreeing with the EDX mapping result. The C 1s spectrum shown in Fig. 2b reveals peaks corresponding to C=C/C–C, C=S, and C=O bonding at 284.8, 286.2, and 289.3 eV, respectively. The existence of sulfur- and oxygen-related bonds indicates that a small amount of sulfur- and oxygen-rich groups is present on the carbon matrix surface. In the Mn 2p spectra

(Fig. 2c), the obvious peaks at 653.4 and 641.6 eV are associated with Mn $2p_{1/2}$ and Mn $2p_{3/2}$, respectively. The minor peak appearing at 664.3 eV is associated with the formation of a C–S–Mn bond between MnS and the carbon skeleton. The formation of the C–S–Mn bond can not only enhance the structural stability, but can also accelerate the charge migration between MnS and the carbon matrix. In the Co 2p spectra (Fig. 2d), the peaks at 781.2 and 797.4 eV can be associated with Co $2p_{3/2}$ and Co $2p_{1/2}$ of Co^{2+}, while the peaks at 778.8 and 797.7 eV can be related to Co $2p_{3/2}$ and Co $2p_{1/2}$ of Co^{3+}. In addition, the peaks sited at 785.2 and 802.8 eV are assigned to two satellite peaks of Co 2p. For the S 2p spectrum (Fig. 2e), the peaks at 163.8 and 165.2 eV can be associated with the C–S–C bond, demonstrating that the S atoms are doped into the carbon framework during sulfurization. The peaks present at 162.1 and 161.0 eV are from the Mn–S bond, while the peaks at 162.6 eV and 161.6 eV are ascribed to the Co–S bond. XPS analysis results reveal that S has been incorporated into the carbon matrix, which can create a variety of defect structures that enhance the sodium storage performance. Combined with the C–S–Mn bond formed between MnS and the carbon skeleton and the heterostructure of MnS and CoS, the MnS/CoS@C11 composite is expected to exhibit exceptional electrochemical properties. Fig. 2f shows the Raman spectra of MnS@C, MnS/CoS@C and CoS@C11, respectively. Two broad peaks of D (disordered domain) and G (graphitic structure) bands can be detected at around 1347 and 1584 cm^{-1}, respectively. According to the fitting results, the D/G intensity ratios of MnS@C, MnS/CoS@C11 and CoS@C are 1.23, 1.30 and 1.69, respectively. Compared with MnS@C and CoS@C, MnS/CoS@C11 has an appropriate amount of defects, which can offer moderate active sites for sodium storage.[30]
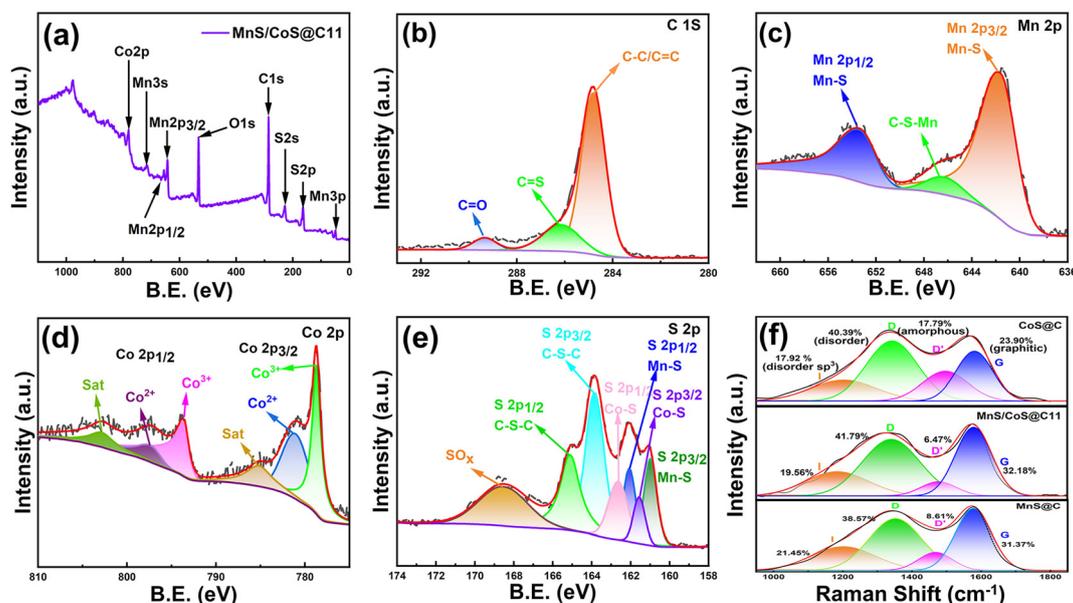

Fig. 2 (a) XPS survey of the MnS/CoS@C11 composite. High-resolution XPS spectra of (b) C 1s, (c) Mn 2p, (d) Co 2p and (e) S 2p of MnS/CoS@C11. (f) Raman spectra of MnS@C, MnS/CoS@C and CoS@C samples.

The electrochemical characteristics of the MnS/CoS@C11 composite and control samples (MnS@C, MnS/CoS@C31, MnS/CoS@C32 and CoS@C) were used as anode materials and evaluated in SIB half-cells. As illustrated in Fig. 3a, the cyclic voltammetry (CV) profiles of the MnS/CoS@C11 composite for the initial three cycles were recorded at a speed of 0.2 mV s^{-1} with a potential range from 0.01 to 3 V (vs. Na$^+$/Na). Two distinct reduction peaks appeared at 0.8 and 0.4 V during the initial sodiation, which later disappeared in the subsequent cycles, corresponding to the electrolyte decomposition and solid electrolyte interface (SEI) formation. The double peaks that appeared at 1.72 V and 2.14 V during the oxidation process might be attributed to the conversion reactions from metallic elements and Na$_2$S to MnS and CoS. The CV profiles for the later cycles are nearly superimposed, indicating the occurrence of a reversible conversion on the MnS/CoS@C11 electrode. As depicted in Fig. S7,† the CV profiles of MnS@C and CoS@C electrodes are also tested for comparison. Fig. 3b demonstrates the galvanostatic charge/discharge (GCD) profiles of the MnS/CoS@C11 electrode at a current of 0.1 A g^{-1} in the 1st, 2nd, and 10th cycles. Obviously, the potential plateaus correspond well to the peak positions in the CV profiles. The GCD profiles of MnS@C, MnS/CoS@C31, MnS/CoS@C32 and

CoS@C are also tested and displayed in Fig. S8.† Moreover, the subsequent cycles overlap well with the second one, demonstrating the excellent cycling performance of the material. The typical GCD profiles of MnS/CoS@C11 at various current densities have been tested and displayed in Fig. 3c. All the profiles show a similar shape, demonstrating excellent cycling stability. The initial discharge/charge specific capacities of the MnS@CoS@11 electrode are 792 and 529.3 mA h g^{-1}, which are equivalent to an initial coulombic efficiency (ICE) of 66.8%. The low ICE could be attributed to the electrolyte decomposition and SEI formation in the first cycle.[25,31] It is noteworthy that the coulombic efficiency was nearly 100% in the subsequent cycles, which should be ascribed to the highly reversible Na$^+$ insertion/extraction process. Moreover, the fast Na$^+$ storage performance of the MnS/CoS@C11 electrode was proved by the rate capability tests (Fig. 3d), and the relevant GCD profiles at various current densities are presented in Fig. 3c. The sodium storage capacities of the MnS/CoS@C11 electrode at current densities of 0.1, 0.5, 1.0, 2.0, 5.0, 8.0 and 10.0 A g^{-1} were 526.1, 498.7, 464.3, 428.6, 383.2, 316.4 and 273.7 mA h g^{-1}, respectively. When the current density was returned to 0.1 A g^{-1}, the capacity was restored to 520.1 mA h g^{-1}, manifesting superior structural stability and excellent
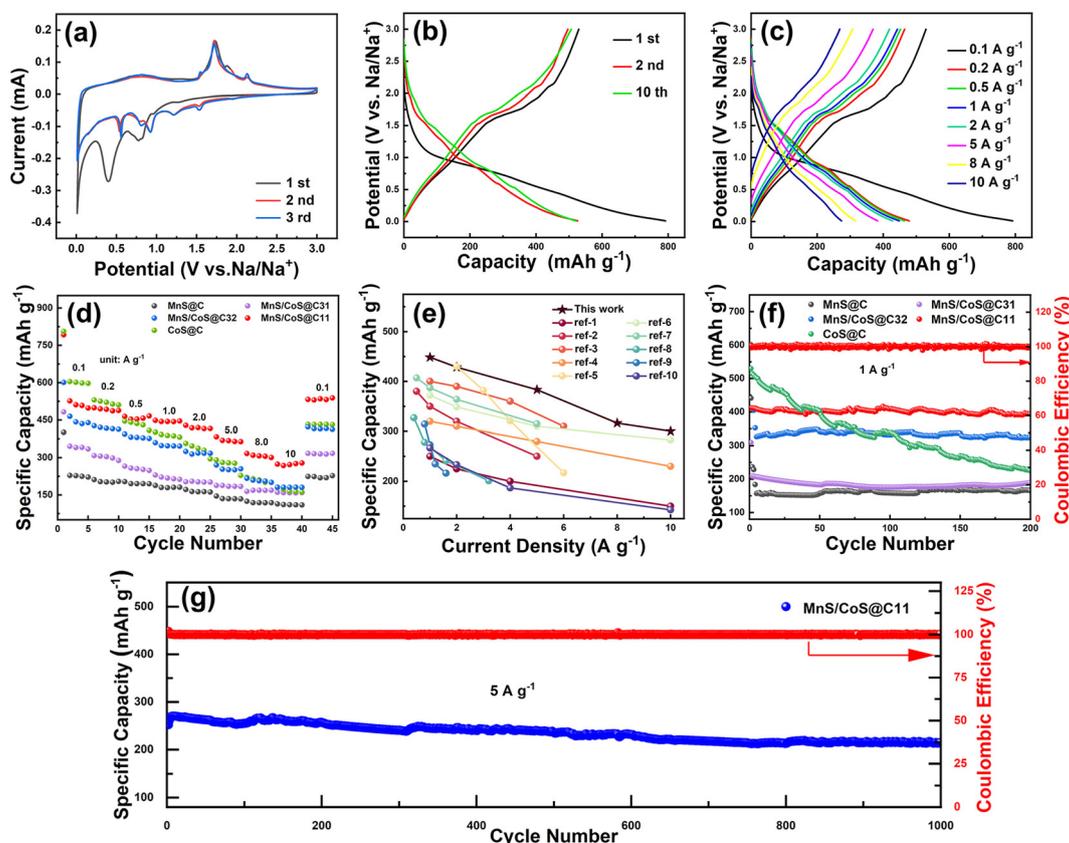

Fig. 3 (a) Initial three CV profiles of MnS/CoS@C11. (b) The 1st, 2nd and 10th GCD profiles of the MnS/CoS@C11 composite. (c) GCD profiles of MnS/CoS@C11. (d) Rate capability test of MnS@C, MnS/CoS@C31, MnS/CoS@C32, MnS/CoS@C11, and CoS@C electrodes. (e) Comparison of rate performance with MnS-based and CoS-based anodes. (f) Cycling performance of MnS@C, MnS/CoS@C31, MnS/CoS@C32, MnS/CoS@C11, and CoS@C electrodes at 1 A g^{-1}. (g) Long-term cycle life of the MnS/CoS@C11 electrode at 5 A g^{-1}.

reversibility for fast sodiation/desodiation. These values are higher than those of MnS@C (224.3 mA h g^{-1}), MnS/CoS@C31 (316.7 mA h g^{-1}), MnS/CoS@C32 (422.2 mA h g^{-1}) and CoS@C (432.5 mA h g^{-1}). The GCD profiles of MnS@C, MnS/CoS@C31, MnS/CoS@C32 and CoS@C with different current densities are also characterized and displayed in Fig. S9.† Fig. 3e shows the rate capability comparison of the MnS/CoS@C11 electrode with other reported MnS-based and CoS-based anodes.[14,32–40] Evidently, the MnS/CoS@C11 electrode possesses superiority in both capacity and rate capability. As depicted in Fig. 3f, the cycling performances of MnS@C, MnS/CoS@C31, MnS/CoS@C32, MnS/CoS@C11 and CoS@C electrodes at 1 A g^{-1} were evaluated. This shows that MnS/CoS@C11 has the best cycling stability and capacity performance. Furthermore, the long-term cycling performance of the MnS/CoS@C11 anode at a high current of 5 A g^{-1} was evaluated and demonstrated in Fig. 3g. Impressively, the MnS/CoS@C11 electrode can maintain a high capacity of 214.8 mA h g^{-1} after 1000 cycles, equivalent to 84.7% capacity retention,

showing excellent cycling durability. The nanostructure of the MnS/CoS@C11 electrode after long-term cycling was characterized by SEM. As observed in Fig. S10,† the octahedral structure of MnS/CoS@C11 can still be preserved.

To further investigate the high-rate performance of MnS/CoS@C11, the CV profiles of MnS@C, MnS/CoS@C11 and CoS@C electrodes were recorded at different scan rates ranging from 0.2 to 2 mV s^{-1} (Fig. 4a and Fig. S11†). As displayed in Fig. 4a, these CV profiles of the MnS/CoS@C11 electrode exhibited similar shapes with slight peak separations, indicating minimal polarization and fast Na$^+$ mitigation at high rates. As previously reported, the correlation between the measured peak current (i) and the scan rate (ν) conforms to the following equation:[41]

$$i = a\nu^b. \tag{1}$$

Configurable parameters a and b are involved in this equation, and the b value has the potential to assess the sodium storage performance. Specifically, $b = 0.5$ indicates
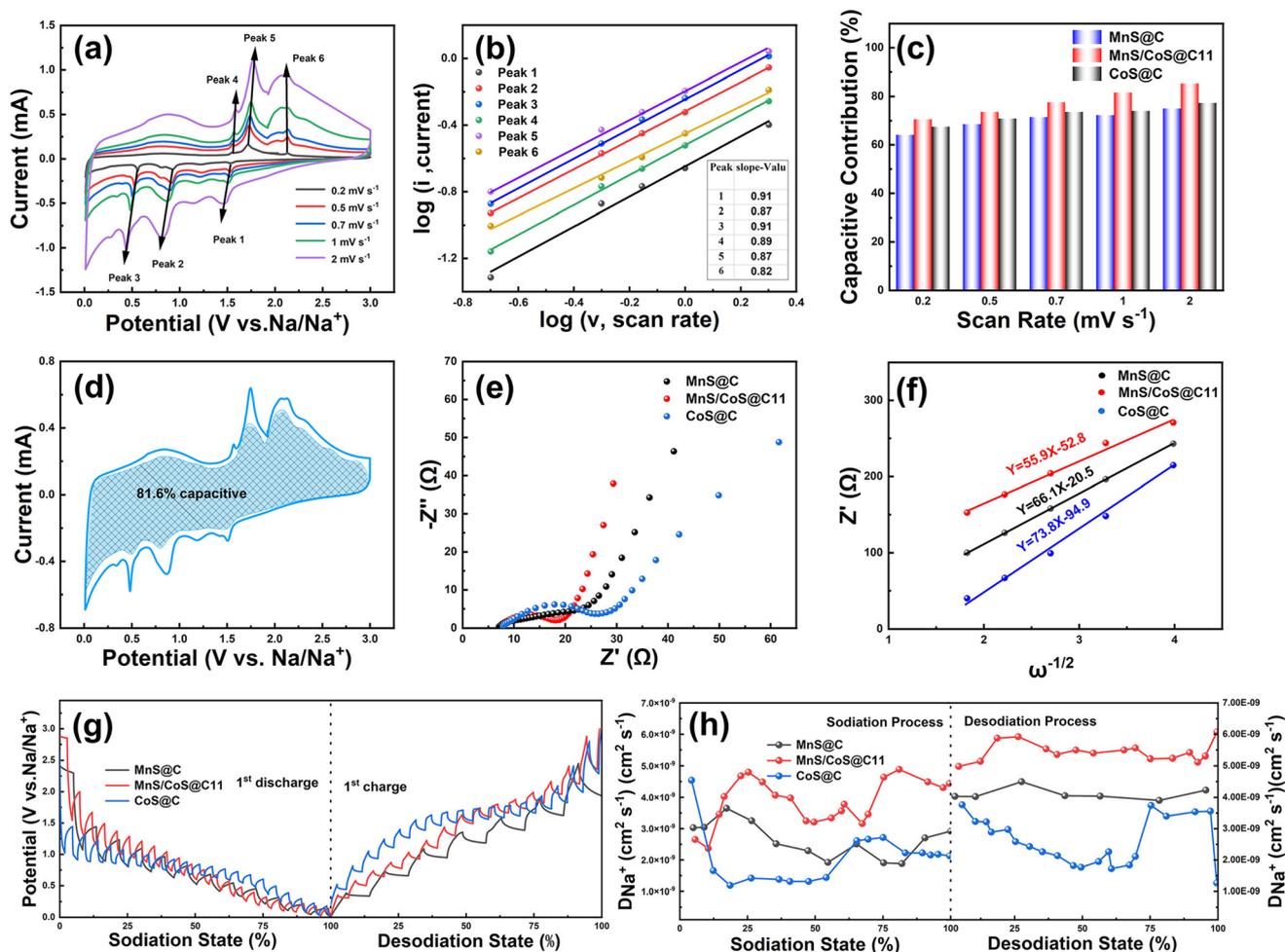

Fig. 4 (a) CV profiles of MnS/CoS@C11 at various speeds. (b) b values of cathodic and anodic peaks for MnS/CoS@C11. (c) Capacitive contribution proportions of MnS@C, MnS/CoS@C11 and CoS@C electrodes at various speeds. (d) Capacitive contribution of the MnS/CoS@C11 electrode at 1 mV s^{-1}. (e) Nyquist plots. (f) The plots of Z' versus $\omega^{-1/2}$ for MnS@C, MnS/CoS@C11 and CoS@C electrodes according to EIS. (g) GITT curves and (h) the corresponding Na$^+$ diffusion coefficients.

battery-like behavior, while $b = 1$ demonstrates capacitor-like behavior.[34,42] For the MnS/CoS@C11 electrode, the b values of anodic and cathodic peaks were 0.91, 0.87, 0.91, 0.89, 0.87, and 0.82 (Fig. 4b), respectively, manifesting that the sodium storage kinetics of MnS@CoS@C11 is dominated by the capacitive-like behavior.[39] The b values of MnS@C and CoS@C electrodes are also calculated and shown in Fig. S12† for comparison. Additionally, the contribution ratio of the capacitive current at a given CV curve can be determined using the following formula:[43]

$$i(V) = k_1 + k_2 \nu^{1/2}. \tag{2}$$

In the above equation, i (mA) and ν (mV s^{-1}) represent the current at a particular potential (V) and sweep rate, respectively. The parameters k_1 and k_2 correspond to the fitting of capacitance and diffusion-controlled contributions. As displayed in Fig. 4c, MnS/CoS@C11 exhibited contribution ratios of 70.5%, 73.6%, 77.3%, 81.6%, and 85.4% at sweep rates of 0.2, 0.5, 0.7, 1, and 2 mV s^{-1}, respectively. These values are larger than those obtained from the MnS@C and CoS@C electrodes, implying faster Na$^+$ transport in the MnS/CoS@C11 electrode. Obviously, the MnS/CoS@C11 electrode exhibits a higher capacitive contribution value than MnS@C and CoS@C electrodes due to the formation of MnS/CoS heterojunctions, which are expected to elevate the charge transfer and accelerate the interfacial reaction. For example, Fig. 4d depicts that 81.6% of the total capacity of the MnS/CoS@C11 electrode comes from the capacitive-controlled contribution at a sweep rate of 1 mV s^{-1}. Hence, the remarkable rate capability of the MnS/CoS@11 electrode could be promoted by the high capacitive contribution.[9]

As illustrated in Fig. 4e, the electrochemical impedance spectroscopy (EIS) plots of MnS@C, MnS/CoS@C and CoS@C electrodes were recorded after three cycles. The Nyquist plots exhibit a consistent pattern, characterized by a semicircle at high frequencies and a straight line at low frequencies. Apparently, compared to MnS/C and CoS/C electrodes, the MnS/CoS@C11 electrode has a smaller semicircle, indicating the lowest charge transfer resistance, which can be ascribed to the internal built-in electric field formed at the MnS and CoS contact interface, which can accelerate the charge mitigation and interfacial reaction kinetics. The Na$^+$ diffusion coefficients could be studied using the Warburg factor (σ) related to the low frequency linear drift slope in eqn (3).[44]

$$Z' = R_e + R_{ct} + \sigma_w \omega^{-1/2} \tag{3}$$

As shown in Fig. 4f, Z'–$\omega^{-1/2}$ curves show that the MnS/CoS@C11 electrode has the lowest slope (55.9), indicating that the Na$^+$ diffusion coefficients of the MnS/CoS@C11 electrode are higher than those of the MnS@C and CoS@C electrodes. The fast Na$^+$ diffusion rate is attributed to the heterojunction between MnS and CoS that can greatly promote the ion mitigation and conductivity of the electrode materials.

The galvanostatic intermittent titration technique (GITT) was employed to evaluate the Na$^+$ diffusion coefficients (D_{Na^+})

during the discharge/charge process. The D_{Na^+} of MnS@C, CoS@C, and MnS/CoS@C11 electrodes can be calculated using the following formula:[45]

$$D = \frac{4L^2}{\pi\tau}\left(\frac{\Delta E_s}{\Delta E_t}\right)^2. \tag{4}$$

The obtained outcomes that correspond to the aforementioned calculations are demonstrated in Fig. 4g and h. Obviously, the D_{Na^+} values of the MnS/CoS@C11 electrode are higher than those of the MnS@C and CoS@C electrodes. The enhanced ionic transport should be ascribed to the internal built-in electric field formed between MnS and CoS, which significantly accelerates the interfacial reaction kinetics and ion/electron migration.

To further gain insight into the underlying sodium storage behavior of MnS/CoS@C11, *in situ* EIS and *ex situ* XRD and XPS were performed. As depicted in Fig. 5a, the Nyquist plots at different potentials were collected and displayed as a 3D image. The intersection with the x-axis at a low frequency represents the solid-state Na$^+$ diffusion resistance (R_s), while the two semicircles at the high frequency are attributed to the charge transfer resistance (R_{ct}) and second-phase impedance (R_f). The impedance changes during the sodiation/desodiation cycle can reflect the electrochemical process to a certain extent. As shown in Fig. 5b, during the discharge/charge process, R_s remains almost unchanged (from 7.1 Ω to 6.8 Ω), indicating that the electrode structure is very stable. In the first sodiation process (from 3.0 V to 0.6 V), the Nyquist plot consists of a semicircle and a diagonal line, demonstrating a single-phase sodium storage behavior. Meanwhile, the R_{ct} value exhibits a slight decrease, indicating facile charge transfer. However, during the sodiation/desodiation process from 0.6 V to 0.01 V and 0.01 V to 0.6 V, the Nyquist plot gradually separates into two semicircles and one diagonal line, displaying a multiphase electrochemical process. In this cycle, the initial R_{ct} value remains stable (from 9.4 Ω to 9.5 Ω). Meanwhile, a new R_f value first increases from 13.9 Ω to 20.1 Ω (from 0.6 V to 0.01 V) and then decreases to 16.9 Ω (from 0.01 V to 0.6 V); these variations demonstrate that the composite mainly undergoes conversion reactions in the low potential range. Significant structural evolution and compositional variations occur at a low potential, resulting in a sluggish ion/electron transfer rate. When charged back from 0.6 to 3.0 V, the Nyquist plots recover to their original shape, manifesting a similar single-phase sodium storage behavior as the initial. Overall, in the first discharge/charge process, the MnS/CoS@C11 electrode suffers from two different impedance variation steps, with the main structural variation occurring at a low potential (below 0.6 V). The corresponding minor changes in the resistance values indicate that the electrochemical reaction is highly reversible.[15]

As shown in Fig. 5c–g, *ex situ* XRD and *ex situ* XPS were characterized under selected potentials. The structural evolution of the MnS/CoS@C11 electrode during Na$^+$ insertion/extraction was determined (Fig. 5d). For the original sample,
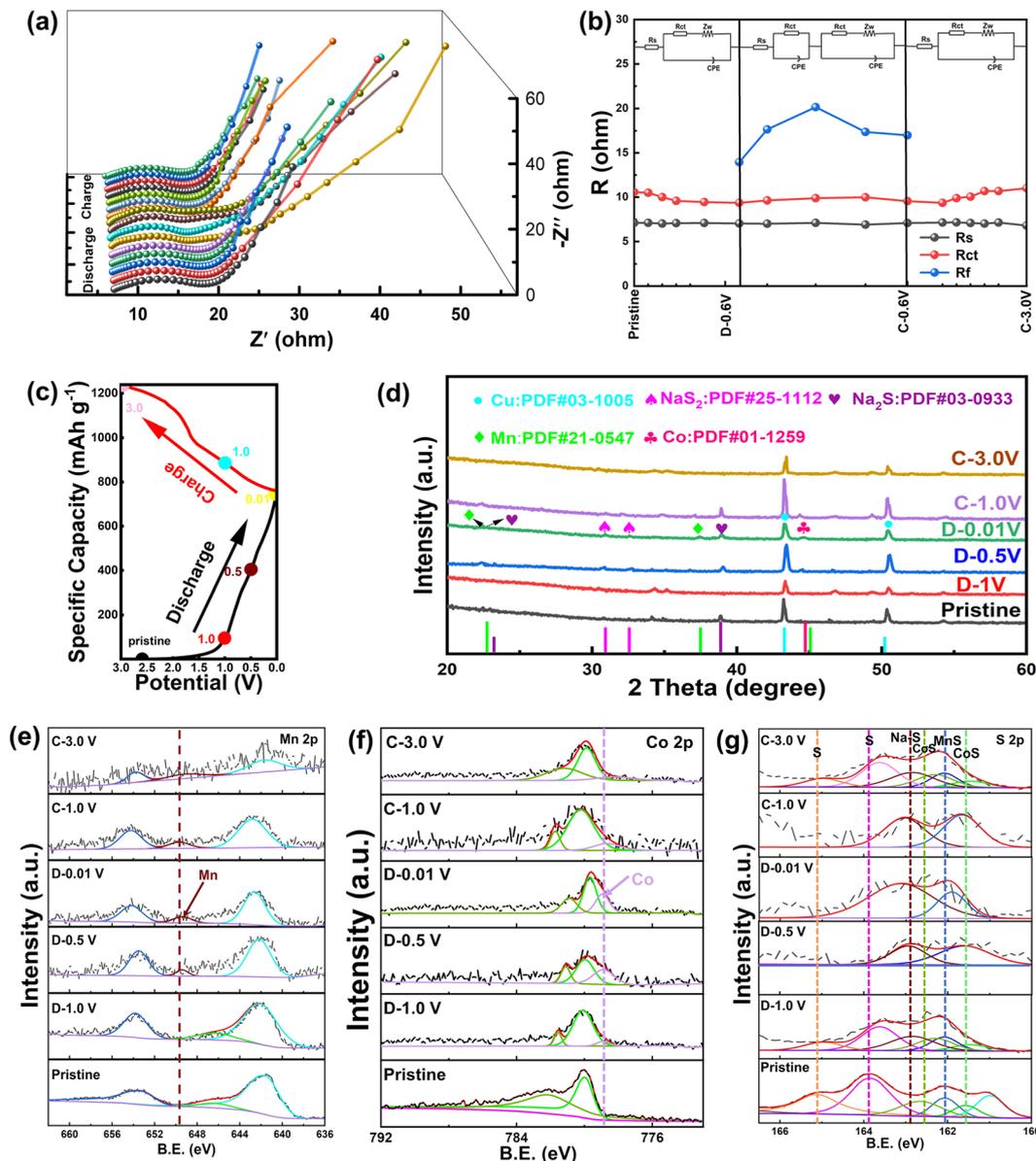
Fig. 5 The sodium storage mechanism analysis of MnS/CoS@C11. (a) The *in situ* EIS measurement at different potentials. (b) Evolution of resistance values in different discharge/charge states. (c) GCD profiles with dots as the selected potential for XRD and XPS tests. (d) *Ex situ* XRD patterns. *Ex situ* XPS spectra of (e) Mn 2p, (f) Co 2p, and (g) S 2p.

diffraction peaks belonging to MnS and CoS were detected. In the following discharge process, the peak intensities of MnS and CoS gradually decreased. Meanwhile, diffraction peaks from Mn, Co, NaS$_2$, and Na$_2$S gradually appeared. As continuously discharged to 0.01 V, the peaks of MnS and CoS vanished, while the peaks of Mn, Co, NaS$_2$, and Na$_2$S became dominant. Moreover, in the reversed charging process, the peaks of Mn, Co, NaS$_2$, and Na$_2$S became progressively weaker. Subsequently, the minor peaks of MnS and CoS can be observed again, demonstrating that the electrochemical reaction between the MnS/CoS heterostructure and Na$^+$ is reversible.[16]

This result can be confirmed by the *ex situ* XPS characterization. Fig. 5e and f show the Mn 2p and Co 2p spectra in different states, respectively. When the potential gradually decreased to 0.01 V, new peaks assigned to Mn^0 and Co^0 appeared at 649.5 and 778.8 eV, respectively, which are ascribed to the electrochemical reaction between Na$^+$ and the MnS/CoS heterostructure. Subsequently, in the S 2p spectra (Fig. 5g), a new Na–S compound peak appeared at 162.7 eV. These results manifest the conversion reaction of the MnS/CoS heterostructure during sodiation. In the subsequent charging process, the peaks of Mn^0 (649.5 eV), Co^0 (778.8 eV) and Na–S compounds (162.7 eV) weakened, but the MnS and CoS peaks are strengthened. When the battery is charged to 3.0 V, the peaks belonging to Mn^0 and Co^0 fully disappear, while the peaks of MnS and CoS almost recover to their pristine position. The *ex situ* XPS results showed that the conversion reac-
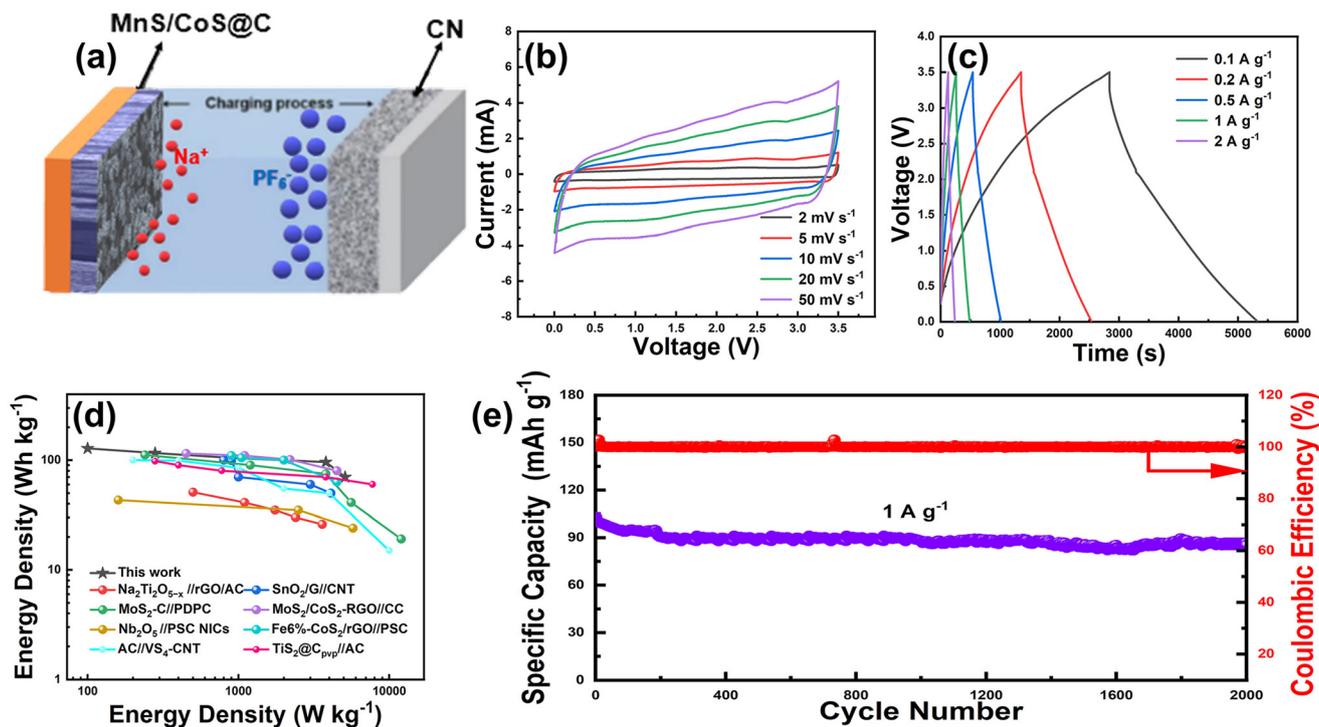
Fig. 6 (a) Schematic of the assembled SIC device. (b) CV profiles of the MnS/CoS@C11//NC SIC at different scan rates. (c) GCD profiles of the MnS/CoS@C11//NC SIC at various current densities. (d) Ragone plots of the SIC in comparison with recently reported SICs. (e) Long-term cycling stability of the NC//MnS/CoS@C11 SIC at 1 A g^{-1}.

tion between the MnS/CoS heterostructure is highly reversible, agreeing well with the *ex situ* XRD result.

To showcase the practical application of MnS/CoS@C11 heterostructures as anode materials, a prototype sodium-ion capacitor (SIC) was constructed. As shown in Fig. 6a, the SIC consists of a MnS/CoS@C11 based battery-type anode and a N-doped carbon nanosheet (NC) based capacitive-type cathode, which is denoted as MnS/CoS@C11//NC. The NC cathode was prepared according to our previous report. The electrochemical properties of the NC cathode were tested and are demonstrated in Fig. S13,† which can yield a high capacity of 71.1 mA h g^{-1} at 1 A g^{-1} and maintain 67.2 mA h g^{-1} at 10 A g^{-1}. To achieve the maximum electrochemical performance, the mass ratio of NC to MnS/CoS@C11 was controlled to 2.5 : 1. The voltage range was adjusted to 0–3.5 V based on the CV curves of various materials to prevent potential electrolyte decomposition and side reactions (Fig. S14†). Fig. 6c depicts the CV profiles of SIC at various sweep rates. As the sweep rate increases, the CV profiles maintain their initial shape without obvious deformation, demonstrating excellent reversibility and rate capability. The slight deviation from the conventional symmetric supercapacitor observed in the CV curves provides evidence for the amalgamation of two distinct charge storage mechanisms in the anode and cathode. Similarly, the GCD curves shown in Fig. 6c also demonstrate a minor deviation from the triangular shape, confirming the coexistence of faradaic and non-faradaic reactions again. The energy density and power density of the SIC were calculated based on the GCD

profiles; the SIC can deliver a maximum energy density of 120.7 W h kg^{-1} at a power of 87.5 W kg^{-1}. Even at an ultra-high power of 12 250 W kg^{-1}, the SIC can still provide an energy density of 29.2 W h kg^{-1}, showing its excellent rate capability. To demonstrate the practical applications of the SIC, a humidity/temperature sensor can be powered by a charged SIC (Fig. S15†). These results are comparable to or even better than most previously reported SICs (Fig. 6d), such as Na$_2$Ti$_2$O$_{5-x}$/rGO/AC (51 W h kg^{-1}), SnO$_2$/G//CNT (103 W h kg^{-1}), Fe6%–CoS$_2$/rGO//PSC (110 W h kg^{-1}), MoS$_2$–C//PDPC (111.4 W h kg^{-1}), MoS$_2$/CoS$_2$–RGO//CC (115 W h kg^{-1}), Nb$_2$O$_5$//PSC NICs (43.2 W h kg^{-1}), AC//VS$_4$–CNT (100 W h kg^{-1}), and TiS$_2$@C$_{pvp}$//AC (98 W h kg^{-1}).[42,46–52] In addition, the MnS/CoS@C11//NC SIC also delivers remarkable cycling stability, maintaining 85% of the initial capacity with almost 100% CE after 2000 cycles at 1 A g^{-1}, showing great potential application in high-power energy storage systems.

Conclusions

To put it briefly, highly distributed MnS/CoS heterostructured nanoparticles encapsulated in an S-doped carbon matrix are synthesized *via in situ* sulfurization of the Mn/Co-MIL-100 MOF. Owing to the MnS/CoS heterojunctions formed inside the MnS/CoS composite, the ion/electron transport is accelerated. Moreover, the carbon framework not only enhances the electronic conductivity but also serves as a cushion for volume

changes, thus reinforcing structural stability. Combining the as-mentioned synergistic effects, the obtained MnS/CoS@C composite displays a high reversible capacity of 526.1 mA h g^{-1} at 0.1 A g^{-1} and remarkable rate capability (273.7 mA h g^{-1} at 10 A g^{-1}). Various analytical methods, including *in situ* EIS, *ex situ* XPS and XRD, reveal that Na^+ storage in MnS/CoS@C involves a highly reversible conversion reaction. By coupling a N-doped carbon nanosheet cathode, the assembled SIC can demonstrate a maximum energy density of 120.7 W h kg^{-1} and a superior power density of 12 250 W kg^{-1}. Overall, the present work provides a viable strategy for designing high-performance heterostructure anode materials for high power sodium-ion based energy storage systems.

Conflicts of interest

There are no conflicts to declare.

Acknowledgements

References

1 S. Liu, W. Liu, D. Ba, Y. Zhao, Y. Ye, Y. Li and J. Liu, *Adv. Mater.*, 2023, **35**, e2110423.

2 Y. Qin, C. Cheng, H. Geng, C. Wang, W. Hu, W. Xu, Z. Shuai and D. Zhu, *Phys. Chem. Chem. Phys.*, 2016, **18**, 14094–14103.

3 V. Palomares, P. Serras, I. Villaluenga, K. B. Hueso, J. Carretero-González and T. Rojo, *Energy Environ. Sci.*, 2012, **5**, 5884–5901.

4 J. Ding, W. Hu, E. Paek and D. Mitlin, *Chem. Rev.*, 2018, **118**, 6457–6498.

5 J. Y. Guo, Z. Y. Zhang, T. Guan, L. W. Mao, Q. Ban, K. Zhao and T. P. Loh, *Chem. Sci.*, 2019, **10**, 8792–8798.

6 J. Yu, X. Li, Y. Sun and X. Liu, *Ceram. Int.*, 2018, **44**, 17113–17117.

7 F. Li, Z. Wei, A. Manthiram, Y. Feng, J. Ma and L. Mai, *J. Mater. Chem. A*, 2019, **7**, 9406–9431.

8 R. Wei, Y. Dong, Y. Zhang, X. Kang, X. Sheng and J. Zhang, *Nano Res.*, 2021, **15**, 3273–3282.

9 S. Chen, J. Zhao, Y. Pang and S. Ding, *Nanotechnology*, 2019, **30**, 425402.

10 F. Han, C. Zhang, B. Sun, W. Tang, J. Yang and X. Li, *Carbon*, 2017, **118**, 731–742.

11 H. Fu, Q. Wen, P. Y. Li, Z. Y. Wang, Z. J. He, C. Yan, J. Mao, K. Dai, X. H. Zhang and J. C. Zheng, *Small Methods*, 2022, **6**, e2201025.

12 Y. Yang, Y. Ma, X. Wang, Z. Gao, J. Yu and T. Liu, *Chem. Eng. J.*, 2023, **455**, 140610.

13 X. Gao, X. Zhang, J. Jiang and J. Chen, *Mater. Lett.*, 2018, **228**, 42–45.

14 N. Fu, Y. Liu, R. Liu, X. Wang and Z. Yang, *Small*, 2020, **16**, e2001607.

15 G. Li, K. Chen, Y. Wang, Z. Wang, X. Chen, S. Cui, Z. Wu, C. Soutis, W. Chen and L. Mi, *Nanoscale*, 2020, **12**, 8493–8501.

16 Y. Lin, Z. Qiu, D. Li, S. Ullah, Y. Hai, H. Xin, W. Liao, B. Yang, H. Fan, J. Xu and C. Zhu, *Energy Storage Mater.*, 2018, **11**, 67–74.

17 B. Jiang, Y. He, B. Li, S. Zhao, S. Wang, Y. B. He and Z. Lin, *Angew. Chem., Int. Ed.*, 2017, **56**, 1869–1872.

18 J. Fei, S. Zhao, X. Bo, F. Xie, G. Li, E. A. M. A. Ahmed, Q. Zhang, H. Jin and Z. Lin, *Carbon Energy*, 2023, e333.

19 F. Xie, S. Zhao, X. Bo, G. Li, J. Fei, E.-A. M. A. Ahmed, Q. Zhang, H. Jin, S. Wang and Z. Lin, *J. Mater. Chem. A*, 2023, **11**, 53–67.

20 Y. Li, J. Qian, M. Zhang, S. Wang, Z. Wang, M. Li, Y. Bai, Q. An, H. Xu, F. Wu, L. Mai and C. Wu, *Adv. Mater.*, 2020, **32**, e2005802.

21 L. Cao, X. Gao, B. Zhang, X. Ou, J. Zhang and W. B. Luo, *ACS Nano*, 2020, **14**, 3610–3620.

22 Y. Q. Wu, H. X. Yang, Y. Yang, H. Pu, W. J. Meng, R. Z. Gao and D. L. Zhao, *Small*, 2019, **15**, e1903873.

23 L. Yue, W. Song, Z. Wu, W. Zhao, L. Zhang, Y. Luo, D. Zheng, B. Zhong, Q. Liu, S. Sun, X. Guo and X. Sun, *Chem. Eng. J.*, 2023, **455**, 140824.

24 S. Wan, M. Cheng, H. Chen, H. Zhu and Q. Liu, *J. Colloid Interface Sci.*, 2022, **609**, 403–413.

25 Q. Lin, S. Zhang, L.-J. Yu, B. Hou, S. Zhang, Z. Wang, J. Song and X. Zhao, *Chem. Eng. J.*, 2023, **455**, 140945.

26 Q. Song, Z. Wu, Y.-X. Wang, S. X. Dou and J. Yang, *Adv. Energy Mater.*, 2023, **12**, 2300739.

27 X. F. Lu, Y. Chen, S. Wang, S. Gao and X. W. D. Lou, *Adv. Mater.*, 2019, **31**, e1902339.

28 Q. Xiong, J. Zheng, B. Liu, Y. Liu, H. Li and M. Yang, *Appl. Catal., B*, 2023, **321**, 122067.

29 J. Zheng, T. Kang, B. Liu, P. Wang, H. Li and M. Yang, *J. Mater. Chem. A*, 2022, **10**, 9911–9921.

30 Y. Deng, J. Zheng, B. Liu, H. Li, M. Yang and Z. Wang, *J. Energy Chem.*, 2023, **76**, 470–478.

31 S. Gao, G. Chen, Y. Dall'Agnese, Y. Wei, Z. Gao and Y. Gao, *Chem. – Eur. J.*, 2018, **24**, 13535–13539.

32 S. Liu, Z. Wang, Q. Hou, X. Zhang, A. Zhang, L. Zhang, P. Wu, X. Zhu, S. Wei and Y. Zhou, *J. Taiwan Inst. Chem. Eng.*, 2020, **110**, 71–78.

33 G. K. Veerasubramani, M.-S. Park, J.-Y. Choi, Y.-S. Lee, S. J. Kim and D.-W. Kim, *ACS Sustainable Chem. Eng.*, 2019, **7**, 5921–5930.

34 Y. Wu, J. Cheng, Z. Liang, T. Qiu, Y. Tang, J. Shi, S. Gao, R. Zhong and R. Zou, *Carbon*, 2022, **198**, 353–363.

35 C. Dong, L. Guo, H. Li, B. Zhang, X. Gao, F. Tian, Y. Qian, D. Wang and L. Xu, *Energy Storage Mater.*, 2020, **25**, 679–686.

36 P. Huang, H. Ying, S. Zhang, Z. Zhang and W.-Q. Han, *Chem. Eng. J.*, 2022, **429**, 132396.

37 X. Lian, N. Xu, Y. Ma, F. Hu, H. Wei, H.-Y. Chen, Y. Wu, L. Li, D. Li and S. Peng, *Chem. Eng. J.*, 2021, **421**, 127755.

38 W. Zhang, Z. Yue, Q. Wang, X. Zeng, C. Fu, Q. Li, X. Li, L. Fang and L. Li, *Chem. Eng. J.*, 2020, **380**, 122548.

39 D. Lan, Y. Zhao, Y. Liu, W. He, N. Zhu and J. Cui, *J. Alloys Compd.*, 2022, **912**, 165083.

40 Q. Liu, S. J. Zhang, C. C. Xiang, C. X. Luo, P. F. Zhang, C. G. Shi, Y. Zhou, J. T. Li, L. Huang and S. G. Sun, *ACS Appl. Mater. Interfaces*, 2020, **12**, 43624–43633.

41 X. Wang, S. Kajiyama, H. Iinuma, E. Hosono, S. Oro, I. Moriguchi, M. Okubo and A. Yamada, *Nat. Commun.*, 2015, **6**, 6544.

42 J. Liu, Y. G. Xu and L. B. Kong, *J. Colloid Interface Sci.*, 2020, **575**, 42–53.

43 C. Zhu, W. Yu, S. Zhang, J. Chen, Q. Liu, Q. Li, S. Wang, M. Hua, X. Lin, L. Yin and R. Wang, *Adv. Mater.*, 2023, **35**, e2211611.

44 X. Hu, Y. Liu, J. Chen, J. Jia, H. Zhan and Z. Wen, *J. Mater. Chem. A*, 2019, **7**, 1138–1148.

45 D. T. Ngo, H. T. T. Le, C. Kim, J.-Y. Lee, J. G. Fisher, I.-D. Kim and C.-J. Park, *Energy Environ. Sci.*, 2015, **8**, 3577–3588.

46 L.-F. Que, F.-D. Yu, K.-W. He, Z.-B. Wang and D.-M. Gu, *Chem. Mater.*, 2017, **29**, 9133–9141.

47 P. Zhang, X. Zhao, Z. Liu, F. Wang, Y. Huang, H. Li, Y. Li, J. Wang, Z. Su, G. Wei, Y. Zhu, L. Fu, Y. Wu and W. Huang, *NPG Asia Mater.*, 2018, **10**, 429–440.

48 R. Wang, S. Wang, X. Peng, Y. Zhang, D. Jin, P. K. Chu and L. Zhang, *ACS Appl. Mater. Interfaces*, 2017, **9**, 32745–32755.

49 H. Li, Y. Zhu, S. Dong, L. Shen, Z. Chen, X. Zhang and G. Yu, *Chem. Mater.*, 2016, **28**, 5753–5760.

50 Y.-G. Xu, J. Liu and L.-B. Kong, *J. Electroanal. Chem.*, 2021, **901**, 115740.

51 Z. Song, G. Zhang, X. Deng, Y. Tian, X. Xiao, W. Deng, H. Hou, G. Zou and X. Ji, *Adv. Funct. Mater.*, 2022, **32**, 2205453.

52 J. Tang, X. Huang, T. Lin, T. Qiu, H. Huang, X. Zhu, Q. Gu, B. Luo and L. Wang, *Energy Storage Mater.*, 2020, **26**, 550–559.